Experimental Implementation and Validation of a Broadband LTI Energy-Maximizing Control Strategy for the Wavestar Device

Demián García-Violini, Yerai Peña-Sanchez, Nicolás Faedo, Christian Windt, Francesco Ferri, and John V. Ringwood, *Senior Member, IEEE*

***Abstract*— This study addresses the experimental validation of a linear time-invariant (LTI) energy-maximizing control strategy for wave energy converters (WECs), applied to a 1/20 scale Wavestar WEC. To fulfill this objective, system identification routines are utilized to compute a mathematical (parametric) model of the input–output dynamics of the device, suitable for control design and implementation. With this parametric model, the so-called LiTe-Con energy-maximizing strategy, recently published in the literature, is designed, synthesized, and tested under irregular wave excitation in the wave basin at Aalborg University. Given that the LiTe-Con requires instantaneous knowledge of the wave excitation effects, estimates are provided by means of an unknown-input Kalman filter, designed in close synergy with the so-called internal model principle. For the experimental assessment, both controller and estimator are directly implemented in a real-time architecture. The performance of the LiTe-Con is evaluated in terms of energy-absorption, showing consistent results with respect to those obtained in numerical simulation, hence validating the LiTe-Con controller in a realistic real-time scenario.**

***Index Terms*— Experimental tests, impedance-matching, linear time-invariant (LTI), optimal control, wave energy.**

I. Introduction

THE energy of ocean waves represents a significant resource that, efficiently harvested, can make a significant contribution to the global renewable energy market [1]. Nonetheless, the current cost of wave energy, driven by device manufacturing, deployment, operation, maintenance, and decommissioning, currently prevents wave energy from being competitive with other (renewable) energy sources [2]. Energy maximizing control strategies (EMCSs), applied to wave energy converters (WECs), can play a decisive role in reducing the cost of energy from ocean waves and, thereby, achieve commercial viability of wave energy technology.

The efficacy of model-based EMCSs is directly affected by the accuracy of the WEC model used during the design stage of the controller. In general, WEC models for the controller design can be divided into two categories, either based on: 1) physical modeling or 2) system identification [3]. EMCSs based on physical modeling are predominant in the wave energy field [4]. The underlying models are commonly based on (the linear) Cummins' equation [5], where the required hydrodynamic parameters are calculated with boundary element method (BEM) solvers. However, due to unmodeled dynamics (e.g., hydrodynamic and mechanical nonlinearities or high-frequency linear dynamics), the robustness of these EMCSs is challenged [6]. Examples of control strategies applied to WECs based on physical modeling can be found in [7] and [8].

EMCSs, based on system identification, can be divided into two subcategories: 1) gray-box identification and 2) black-box identification. Gray-box identification employs a model structure, inspired, for instance, by the broad characteristics of the physical model. The system parameters are tuned using observed data, stemming usually from experimental [9]–[11] or numerical wave tank tests [12]. When the model structure is completely unknown (only considering general assumptions, such as linearity or passivity), and the identification is solely based on observed data, the approach is known as black-box identification. Generally, when accurate *a priori* knowledge of the system structure is not available, black-box approaches allow a more accurate model description compared to gray-box approaches, due to their greater parametric freedom, but may have reduced intuitive appeal since the model structure is relatively disconnected from the physical system.

Following a black-box identification procedure, this study presents the experimental implementation and validation of the recently proposed linear time-invariant controller (LiTe-Con) [13]. Thereby, this study presents the first physical implementation and assessment of the LiTe-Con. Note that, based on a black-box approach, which avoids the need for

Manuscript received November 10, 2020; accepted January 8, 2021. Date of publication January 28, 2021; date of current version October 8, 2021. Manuscript received in final form January 14, 2021. This work was supported by the European Union Horizon 2020 Framework Programme (H2020) under Grant Agreement 731084. The work of Demián García-Violini, Yerai Peña-Sanchez, Nicolás Faedo, and Christian Windt was supported by the Science Foundation Ireland under Grant 13/IA/1886. Recommended by Associate Editor T. Oomen. *(Corresponding author: Demián García-Violini.)*

Demián García-Violini is with the Departamento de Ciencia y Tecnología, Universidad Nacional de Quilmes, Buenos Aires B1876, Argentina (e-mail: ddgv83@gmail.com).

Yerai Peña-Sanchez, Nicolás Faedo, Christian Windt, and John V. Ringwood are with the Centre for Ocean Energy Research, Maynooth University, Maynooth W23 F2H6, Ireland (e-mail: yerai.pena.2017@mumail.ie; nicolas.faedo.2017@mumail.ie; christian.windt.2017@mumail.ie; john.ringwood@eeng.nuim.ie).

Francesco Ferri is with the Department of Civil Engineering, Aalborg University, 9220 Aalborg, Denmark (e-mail: ff@civil.aau.dk).

Color versions of one or more figures in this article are available at https://doi.org/10.1109/TCST.2021.3052479.

Digital Object Identifier 10.1109/TCST.2021.3052479

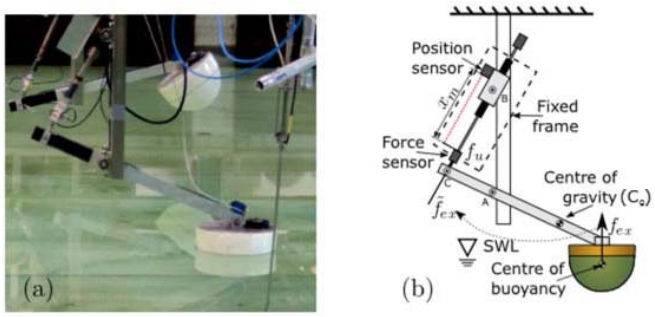

Fig. 1. (a) Photograph of the WEC system employed in the wave basin. (b) Schematic of the experimental WEC system with the dimensions listed in Table I.

a priori information, the presented methodology is designed to be as general as possible, extending its applicability to the widest range of physical platforms, even under the presence of unknown dynamics. Thus, the considered approach is more suitable for scenarios such as the one presented in this study, where only general assumptions, such as linearity, are considered. Conversely, gray-box approaches should not be considered under scenarios where the complete system structure is not accurately known *a priori*. Alternatively, although is beyond the scope of this study, some identification problems can be addressed by combining both approaches, using a gray-box and a black-box approach for the parametric and nonparametric structures of the model [14], [15], respectively. The data for the system identification procedure stem from physical wave tank data acquired in the wave basin at Aalborg University. The system under investigation, as shown and schematically depicted in Fig. 1(a) and (b), respectively, is a 1/20th scale model of a single floater of the Wavestar WEC [16], inspired by the International WEC Control Competition (WECCCOMP) [17], [18]. The particular system is well established and has been extensively studied both numerically [19], [20] and experimentally [9], [21]. With the focus on experimental control studies applied to WEC systems, the approaches presented in [10] and [22] show experimental implementations of EMCSs applied to WECs. However, both [10] and [22] use physical modeling-based approaches for the controller development, while optimization-based control strategies are employed, as commonly proposed in the literature of WEC systems [4]. In addition, an optimization-based model predictive control strategy is compared in [22], with resistive and reactive control approaches, which are commonly considered for WEC systems [13]. Regarding the considered control approach, in [23], an alternative EMCS is proposed that, similar to the LiTe-Con, is essentially an impedance-matching-based EMCS. However, unlike the LiTe-Con controller, the strategy proposed in [23] is presented in the feedback form and does not consider constraints.

In contrast to the LTI control strategy employed in this study, optimization-based controllers, such as model predictive-based [4], moment-matching-based [24], or spectral/pseudospectral-based controllers [25], are predominant in the WEC control literature due to their optimal solutions even in constrained scenarios [4]. However, the implementation of such techniques can be challenging [4]. The LiTe-Con, with fixed parameters, is tuned to approximate the frequency-domain energy-maximizing optimal condition, given by the panchromatic impedance-matching principle, providing a broadband energy maximizing control method. Thereby, the LiTe-Con is simple in its implementation but potentially delivers suboptimal performance when operating under physical device constraints. In addition, the LiTe-Con has the added advantage that only wave excitation force estimation, but no forecasting, is required. Finally, with regard to the LiTe-Con, it is worth mentioning that, to date, among the set of controllers based on the impedance-matching principle for panchromatic cases, only the LiTe-Con and the controller reported in [26] have the added ability to handle constraints [27]; thus, this study is the first one presenting the validation of the LiTe-Con in an experimental setting.

In this study, system identification tests, by means of forced oscillation excitation with chirp-type input signals, are conducted initially. Based on the acquired data, the control design model is identified, and the LiTe-Con is synthesized. Furthermore, based on the identified model, a Kalman-based observer [28] is designed for wave excitation force estimation [29]. Subsequently, for controller validation, the discretized versions of the controller and estimator are implemented using the MATLAB/Simulink xPC-Target environment [30].

The performance of the estimator is evaluated for three different sea states considered in this study, to assess the quality of the excitation force estimates which the LiTe-Con crucially depends on. Subsequently, the performance of the controller is evaluated in terms of power absorption, constraint satisfaction, and fulfillment of (theoretical) optimality conditions. For comparative purposes, using both the identified WEC model and the designed controller, performance is also evaluated using a purely simulated environment.

Note that the proposed system identification and controller design procedure is presented in a general form, such that its application is not restricted to the specific model and/or observed data shown in the case study.

Within this framework, the main contribution of this article, is the validation of the real-world performance of the LiTe-Con WEC controller presented in [13], considering that this study represents the first implementation in an experimental environment of this control strategy. On the other hand, arising from the obtained experimental results, this article illustrates the implementation of a generalizable energy maximizing control technique for WECs, while, at the same time, the simplicity and effectiveness, in terms of implementation and performance, respectively, of the LiTe-Con are shown. Furthermore, the fact that the model used for the control system design is obtained by means of identification strategies, showing the benefit of this approach for WEC systems, constitutes a further contribution of this study. Finally, the strong connection between estimation and control performances of WEC systems is experimentally evaluated in this study.

The remainder of this article is organized as follows. Section II describes the details of the WEC system, as well as the controller/estimator hardware and software architecture employed in this study. Section III details the identification

methodology employed to characterize the force-to-position and force-to-velocity mappings. Section IV shows the LiTe-Con basics, while, in Section V, the LiTe-Con and the estimator design are presented, which also includes a discussion of the controller implementation. The controller performance is then assessed in Section VI, and conclusions are drawn in Section VII.

A. Notation

Throughout this study, $Z(\omega)$ and $z(t)$ denote a Fourier transform pair, while $Z^{\star}(\omega)$ denotes the complex conjugate of $Z(\omega)$. $\mathrm{Re}\{\cdot\}$ and $\mathrm{Im}\{\cdot\}$ denote the real- and imaginary-part operators, respectively. The symbol $\mathbb{I}_n$ denotes the identity matrix of $\mathbb{C}^{n\times n}$.

II. Wavestar WEC, Hardware Environment, and System Description

This section briefly describes the WEC prototype, the hardware, and the software environment utilized in this study.

A. Wavestar WEC System

The prototype system considered in this study, as shown in Fig. 1(a), is based on the Wavestar WEC. The device consists of a hemispherical hull with a single operational degree of freedom (DoF) in pitch. On the full-scale device, the hydraulic power take-off (PTO) system consists of a cylinder, pumping fluid through a generator, with a rated power of 500 kW, for a device with 20 floaters [31]. Here, a single 1:20th scale model of the full-scale device is considered, with an electrical, direct drive, and actuator PTO, inspired by the case study for the International WEC Control Competition (WECCCOMP) [17], [18].

1) System and Hardware Architecture: A schematic of the WEC system is depicted in Fig. 1(b). The floater is connected to the fixed reference frame through two joints (joints A and B). In its equilibrium position, the floater's arm stands at approximately 30° with respect to the horizontal reference plane. Joint C is mobile and has a translational displacement indicated with x_m, which represents the position of the PTO system and is measured using the position laser sensor. Specifically, the system is equipped with the following hardware.

1) *Linear Motor and Driver:* LinMot Series P01-37 × 240F and LinMot E1200 with a force rating of up to ±200 N.
2) *Force Sensor:* S-beam Futek LSB302 300lb load cell with SGA Analog Strain Gauge Amplifier.
3) *Position Laser Sensor:* MicroEpsilon ILD-1402-600.
4) *Input/Output Board:* Data Acquisition Board National Instruments NI PCI-6221 DAQ.

The relevant dimensions and mechanical properties of the system are listed in Table I.

2) Physical Wave Tank: The experimental data, used within this study, were acquired during physical wave tank tests in the wave basin at Aalborg University. A schematic of the wave basin, including all relevant dimensions, is shown in Fig. 2. The tank measures 14.6 m in length and 13 m in width. The water depth of the wave tank was set to 0.9 m. Waves are generated using 30 individually controlled VTI wave paddles (although, for these experiments, the tank was operated as a flume, with all paddles operating in unison). The device is mounted on a gantry spanning the full width of the tank. A photograph of the tank is shown in Fig. 3.

TABLE I
Model Dimensions, Relative to the Still Water Level (SWL), and Mass Properties for the 1/20th Scale Wavestar Device

Parameter	Value	[Unit]
Float Mass	3.075	[kg]
Float MoI (at C_g)	0.001450	[kg·m^2]
Float Draft	0.11	[m]
Float Diameter (at SWL)	0.256	[m]
Arm Mass	1.157	[kg]
Arm MoI (at C_g)	0.0606	[kg·m^2]

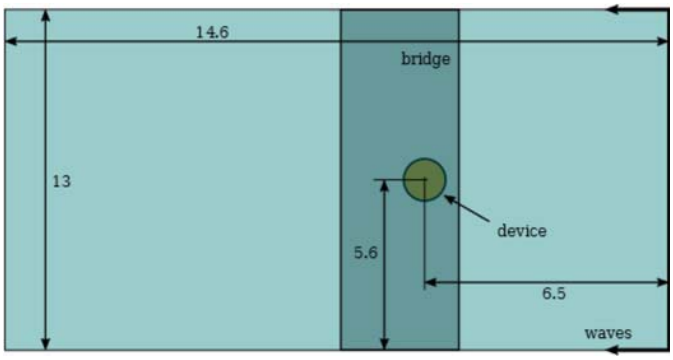

Fig. 2. Sketch with the approximate dimensions (in meters) of the physical wave tank. The orange circle represents the WEC system.

Fig. 3. Photograph of the physical wave tank. Waves are generated with 30 wave paddles.

3) Input–Output Data Acquisition and Computer Hardware: In this study, the data acquisition is implemented using a rapid control prototyping (RCP) hardware architecture, in which the controller is implemented in real time. The RCP architecture has been implemented in the MATLAB/Simulink (version 2015b), using the xPC-Target environment. The RCP architecture is sketched in Fig. 4.

The WEC is interfaced to the target PC via a National Instruments Input/Output board. The target PC runs a real-time operating system (OS) and embeds the controller developed in this study. The sampling frequency of the target PC is 1 kHz (sampling rate $T_m = 10^{-3}$ s), and the target and host PCs communicate through a local Ethernet connection. The LiTe-Con is programed, compiled on the host PC, and then download to the target PC as a compiled code segment. Once running, the controller parameters are accessible (modifiable) from the host PC.

The lower part of Fig. 4 represents the high-level Simulink block diagram, programed in the target PC, which shows how

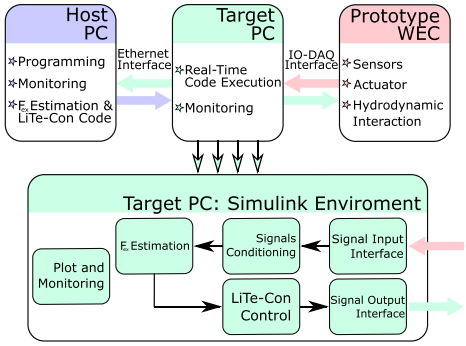

Fig. 4. General software and hardware architecture. The host and target PCs software are detailed. The bottom part details the target PC software environment.

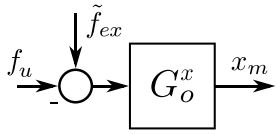

Fig. 5. Block diagram of the simplified WEC model.

the measurements from the hardware are collected and sent through the signal conditioning block.

B. Model Variable Transformation

To avoid the representation of mechanical nonlinearities, due to the rotational DoF, in the identified model (see Section III), only the linear displacement along the PTO axis x_m is considered in this study. Thus, translational forces, instead of torques, are considered throughout the following sections. Thus, avoiding the use of a rotational approach, the system can be described using a linear dynamical structure. Consequently, using the transformed representation of the system, which essentially defines an alternative reference system, the model complexity is significantly simplified. Considering only translational motion along the PTO axis, the WEC system can be schematically depicted as a linear translational system, subject to an excitation force, $\tilde{f}_{\text{ex}}(t)$, representing the wave excitation force, $f_{\text{ex}}(t)$, acting on the device hull [see Fig. 1(b)]. For energy maximization control, a bidirectional external control force $f_u(t)$ is applied along the PTO axis. This reduced model is marked by the black-dashed box in Fig. 1(b).

Fig. 5 shows the block diagram system representation used for the energy maximizing control approach, in which G_o^x represents the force-to-position mapping, considered as

$$G_o^x(s) = C(s\mathbb{I}_n - A)^{-1}B \tag{1}$$

and

$$\begin{cases} \dot{x} = Ax + B(\tilde{f}_{\text{ex}} - f_u) \\ x_m = Cx. \end{cases} \tag{2}$$

With that, the force-to-velocity mapping, commonly considered for energy maximizing control problems [1], [32], can be analytically computed using the system matrices involved in (1) as

$$\dot{x}_m = v_m = CAx + CB(\tilde{f}_{\text{ex}} - f_u). \tag{3}$$

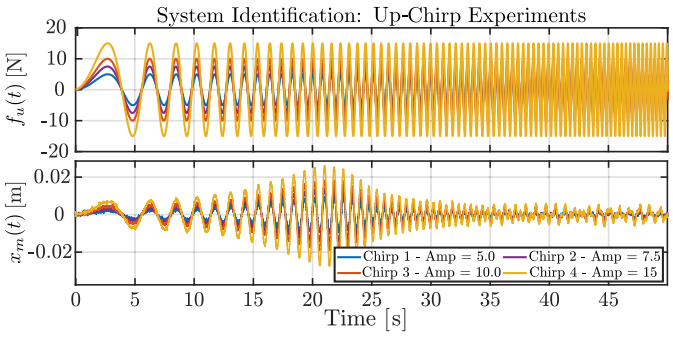

Fig. 6. Up-chirp experiment. The control force (input) $f_u(t)$ and the motor position $x_m(t)$ are plot in the upper and lower plots, respectively.

Note that, as for the force-to-position mapping $G_o^x(s)$, as defined in (1), the force-to-velocity mapping, $G_o^v(s)$, can be equivalently defined based on (3) but is not shown here, for brevity.

III. System Identification

As mentioned in Section I, the model used for the control design is obtained using a black-box identification methodology, where the observed data are taken from chirp experiments performed on the physical system. It should be noted that the identification methodology described in the following is not restricted to observed data from experimental measurements only but can also utilize numerical models, as described in, for example, [12]. For the force-to-position system identification, using the force actuator and position sensor described in Section II-A, a set of classical up-chirp experiments (i.e., with increasing frequency) is performed, where the system is forced into motion by the chirp control force, while $f_{\text{ex}}(t) = \tilde{f}_{\text{ex}}(t) = 0$, i.e., no incident waves are present.

Knowing the approximate location of the natural resonance frequency of the system *a priori*, the control force $f_u(t)$ is defined as a linear frequency sweep in the range [0.1, 60.0] (rad/s) (covering the resonance frequency of the system with a decade below and above), with amplitudes contained in the set $\mathcal{A} = \{5, 7.5, 10, 15\}$ N. The input and output time-traces, of the up-chirp experiments, are shown in Fig. 6.

Using the chirp control force $f_u^i(t)$ signal and the corresponding generated output, $x_m^i(t)$, with $i \in \{1, 2, 3, 4\}$, where the index i indicates the experiment number defined in accordance with each element of the set of amplitudes $\mathcal{A}$, an empirical transfer function estimate (ETFE), $G_i^x(\jmath\omega)$, is computed as follows:

$$G_i^x(\jmath\omega) = \frac{X_m^i(\jmath\omega)}{F_u^i(\jmath\omega)}. \tag{4}$$

To improve the fit between the identified and the empirical model (based on experimental data), where each component of the frequency response is considered as a stochastic process with corresponding mean and variance values, the average frequency response, $\bar{G}^x(\jmath\omega)$, is computed to build a low-variance set, used as the input to the frequency-domain identification algorithm [3]

$$\bar{G}^x(\jmath\omega) = \frac{1}{4}\sum_{i=1}^{4} G_i^x(\jmath\omega). \tag{5}$$

Considering the state-space representation of the WEC model defined in (1), the identification of the force-to-position mapping is performed using a subspace system identification algorithm [3]. Using the force-to-position data obtained in the experimental identification stage and considering the expression in (3) lead to

$$\bar{G}^{v}(\jmath\omega) = \jmath\omega\bar{G}^{x}(\jmath\omega). \tag{6}$$

Note that the expression in (6), which describes a physical mapping, can be indistinctly applied to $G_i(\jmath\omega)$, $\bar{G}(\jmath\omega)$, or $G_o(\jmath\omega)$, considering in each case position or velocity, denoted by the superscripts x or v, respectively. In order to define the most suitable model order n_o, the normalized root mean square accuracy (NRMSA), i.e., the complement of the normalized root mean square error (NRMSE), between the experimental data, $\bar{G}^{x}(\jmath\omega)$ and $\bar{G}^{v}(\jmath\omega)$, and the frequency response of the identified model with order n_o, is computed. Two eight-order nominal linear models, $G_o^{x}(s)$ and $G_o^{v}(s)$, are chosen for the force-to-position and force-to-velocity systems, respectively, obtaining an accuracy greater than 96.5% for both cases. It is worth mentioning that $n_o = 8$ results in an optimal order, in the sense that accuracy values less than 96% were obtained when smaller or larger values of n_o are considered. In addition, the resulting numbers of zeros for $G_0^{x}(s)$ and $G_0^{v}(s)$ are 7 and 8, respectively. The resulting ETFE (magnitude and phase) for the force-to-position $G_i^{x}(\jmath\omega)$ and force-to-velocity $G_i^{v}(\jmath\omega)$ [computed using (6)] mappings, with $i \in \{1, 2, 3, 4\}$, is shown in Fig. 7(a) and (b), respectively. $G_i^{x}(\jmath\omega)$ is indicated with light-blue dotted lines and $G_i^{v}(\jmath\omega)$ with light-orange dotted lines.

From the results for $G_i^{x}(\jmath\omega)$ and $G_i^{v}(\jmath\omega)$, a clear linear response of the analyzed physical system can be observed with small variations in the frequency response of the ETFEs for the different amplitudes defined in $\mathcal{A}$. In addition, according to (5) and (6), the averaged force-to-position mapping, $\bar{G}^{x}(\jmath\omega)$, and averaged force-to-velocity mapping, $\bar{G}^{v}(\jmath\omega)$, are shown in Fig. 7(a) and (b), respectively, using a dashed-black lines. The identified systems $G_o^{x}(s)$ and $G_o^{v}(s)$ are shown in Fig. 7(a) and (b), respectively, using a blue solid line for $G_o^{x}(s)$ and solid-orange line for $G_o^{v}(s)$. Note that, although a precise uncertainty analysis is beyond the scope of this study, from the results shown in Fig. 7, it can be seen that the uncertainty level is higher in the upper and lower ranges of the spectrum, in comparison with the midrange, for both the identified frequency responses and the ETFEs.

For the following discussion, it is worth mentioning that the positive-realness condition, which is verified by the physical system, is neither required in the design of the controller nor the wave excitation force estimator.

IV. LiTe-Con

The energy maximizing control problem for the considered WEC system, stated as the maximization of absorbed energy subject to a set of constraints, can be generally posed as

$$\begin{aligned} &\max_{f_u} \int_0^t v_m(\tau)\, f_u(\tau)\, d\tau \\ &\text{s.t. } \dot{\mathbf{x}}(t) = \mathbf{f}(\mathbf{x}(t),\, f_u(t),\, \tilde{f}_e(t)) \\ &\quad \{\mathbf{x}(t),\, f_u(t)\} \subset \mathcal{C} \end{aligned} \tag{7}$$

where the mapping $\mathbf{f}$ fully describes the time-domain WEC dynamics with $\mathbf{x}$, f_u, and $\tilde{f}_e$ the state vector, control force, and wave excitation force, respectively. The region $\mathcal{C}$ represents the set of constraints defined by the device and actuator (physical) limitations and the system velocity v_m, as defined in (3), which is obtained as a function of the state vector $\mathbf{h}(\mathbf{x})$.

With the aim of maximizing the absorbed energy, the LiTe-Con, as proposed in [13], is based on the fundamental philosophy of impedance-matching [32] but is extended to the panchromatic case. Using system identification algorithms, the controller is synthesized to approximate the frequency domain energy maximizing optimal condition, providing a broadband EMCS. In addition, a suboptimal constraint handling mechanism is implemented.

The LiTe-Con, following the derivation presented in [13], can be defined using the nominal force-to-velocity mapping $G_o^{v}(s)$, as defined in (3) and depicted in Fig. 7(b). For the analytical derivation of the controller, using the real and imaginary part operators (see Section I-A), the force-to-velocity frequency-response can be expressed as

$$G_o^{v}(s)\big|_{s=\jmath\omega} = \mathrm{Re}\{G_o^{v}(\jmath\omega)\} + \jmath\,\mathrm{Im}\{G_o^{v}(\jmath\omega)\}. \tag{8}$$

Then, the well-known optimal feedback controller [32], which guarantees the impedance matching principle of optimality, is given by

$$\mathcal{K}_{\mathrm{fb}}(s)|_{s=\jmath\omega} = \frac{1}{\mathrm{Re}\{G_o^{v}(\jmath\omega)\} - \jmath\,\mathrm{Im}\{G_o^{v}(\jmath\omega)\}}. \tag{9}$$

Using (9), the optimal mapping $T^{\mathrm{opt}}_{\tilde{f}_{\mathrm{ex}}\to v_m}(\omega)$ from $\tilde{F}_{\mathrm{ex}}(\omega)$ to the so-called optimal velocity profile $V_m^{\mathrm{opt}}(\omega)$ can be expressed, in the frequency domain, as

$$\mathcal{T}^{\mathrm{opt}}_{\tilde{f}_{\mathrm{ex}}\to v_m}(\jmath\omega) = \frac{\mathrm{Re}\{G_o^{v}(\jmath\omega)\}^2 + \mathrm{Im}\{G_o^{v}(\jmath\omega)\}^2}{2\mathrm{Re}\{G_o^{v}(\jmath\omega)\}} \tag{10}$$

which implies that, since the mapping expressed in (10) defines a purely real frequency dependent mapping, a zero-phase shift ("phase locking") between $\tilde{F}_{\mathrm{ex}}(\omega)$ and the optimal velocity profile, $V_m^{\mathrm{opt}}(\omega)$, exists. Please note that the issue of "phase locking" at multiple frequencies is not easily described, as discussed in the following. For monochromatic waves, a condition for optimality (max. power capture) is that the device velocity is in phase with the excitation force (see [2]). For panchromatic seas, within the environment of this study, the term "phase locking" denotes the broad time synchronization of velocity and excitation force signals.

However, the intrinsic noncausality of $\mathcal{K}_{\mathrm{fb}}(s)$ in (9), which is presented in the literature as the impedance-matching solution to WEC energy maximizing control problems, does not allow practical implementation of the controller. In addition, from a sensitivity/robustness perspective, the real-world applicability of the controller in (9) has been questioned in [6].

To deal with the intrinsic limitations related to the noncausality, based on the impedance-matching control structure presented in (9), using (8)–(10), the impedance-matching control problem can be formulated into a feedforward control

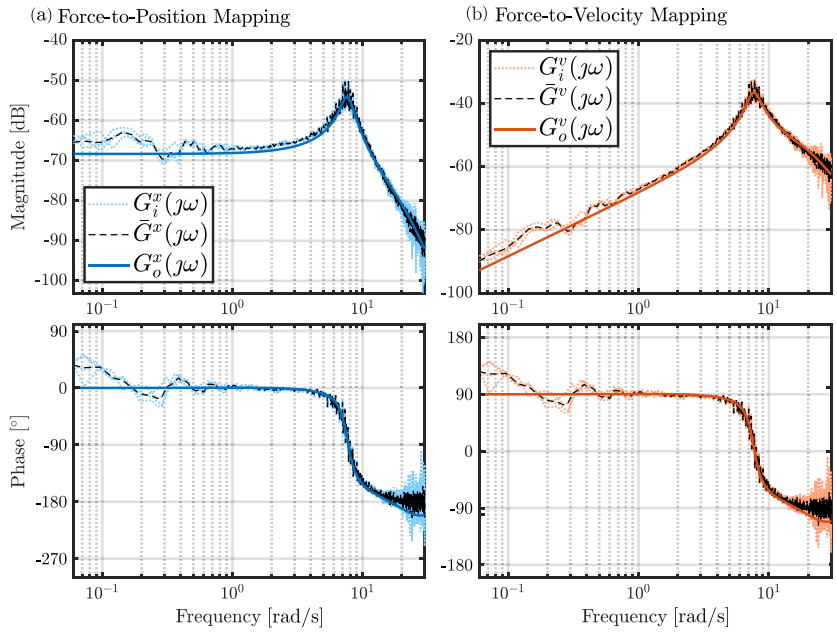

Fig. 7. (a) Force-to-position and (b) force-to-velocity ETFE $H^x(\jmath\omega)$ using amplitudes 5, 7.5, 10, and 15 N. The dotted lines indicate the results for the individual force amplitude, with the according average marked with a dashed line. The identified system is marked with a solid line.

structure. The required feedforward controller is obtained as

$$\mathcal{K}_{\text{ff}}(\jmath\omega) = \frac{\text{Re}\{G_o^v(\jmath\omega)\} + \jmath\text{Im}\{G_o^v(\jmath\omega)\}}{2\text{Re}\{G_o^v(\jmath\omega)\}}. \tag{11}$$

Thus, using the theoretical feedforward control structure presented in (11), the resulting optimal force-to-velocity mapping matches that obtained in the feedback case, as expressed in (10).

The method presented in [13] proposes the approximation of $\mathcal{K}_{\text{ff}}(\jmath\omega)$ with a linear time-invariant-stable (LTI-stable) and implementable dynamical system $K_{\text{ff}}(s)$, such that

$$K_{\text{ff}}(s)|_{s=\jmath\omega} \approx \mathcal{K}_{\text{ff}}(\jmath\omega) \tag{12}$$

where $K_{\text{ff}}(s)$ is obtained using additional frequency-domain system identification algorithms (see [13]).

It is important to note that, in contrast to the feedback case in (9), which, as previously discussed, is unimplementable in real applications, in the feedforward control structure, as presented in (12), estimation of the wave excitation force is required. However, for analytical derivation of the feedforward controller, perfect knowledge of the excitation force is assumed via

$$\tilde{f}_{\text{ex}}(t) = \hat{\tilde{f}}_{\text{ex}}(t) \tag{13}$$

where $\hat{\tilde{f}}_{\text{ex}}(t)$ represents an excitation force estimate.

Then, assuming perfect knowledge of the excitation force, the control force (in the frequency domain) is expressed as

$$F_u(\jmath\omega) = K_{\text{ff}}(\jmath\omega)\tilde{F}_{\text{ex}}(\jmath\omega). \tag{14}$$

The resulting control structure is shown in Fig. 8. Note that in Fig. 8, as in the real implementation case, an estimate of the wave excitation force resulting at joint C [see Fig. 1(b)] is used as the input to the controller $K_{\text{ff}}(s)$.

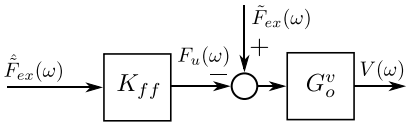

Fig. 8. Feedforward control structure.

V. Design and Implementation

In this study, $\mathcal{K}_{\text{ff}}(\jmath\omega)$ is approximated using a moment-matching-based system identification approach proposed in [33], using five matching points, obtaining, therefore, a tenth-order LTI stable system $K_{\text{ff}}(s)$. For the approximation, in order to consider a smoother data set, the target optimal controller frequency response is generated considering the identified system $G_o^v(\jmath\omega)$

$$K_{\text{ff}}(\jmath\omega) \approx \frac{\text{Re}\{G_o^v(\jmath\omega)\} + \jmath\text{Im}\{G_o^v(\jmath\omega)\}}{2\text{Re}\{G_o^v(\jmath\omega)\}}. \tag{15}$$

The approximation results (magnitude and phase) for the optimal-feedforward controller, $K_{\text{ff}}(\jmath\omega)$, and the resulting optimal mapping, $\mathcal{T}^{\text{opt}}_{\tilde{f}_{\text{ex}}\to v_m}(\jmath\omega)$, are shown in Fig. 9(a) and (b), respectively. Considering (10)–(12), Fig. 9 shows the results, for the controller frequency response [see Fig. 9(a)] and the resulting force-to-velocity mapping [see Fig. 9(b)], considering the average ETFE $\bar{G}^v(\jmath\omega)$, the identified force-to-velocity mapping $G_o^v(s)$, and the resulting controller $K_{\text{ff}}(\jmath\omega)$, which is the implemented controller, using black dotted, orange dashed, and blue solid lines, respectively. Note that, for the plots in Fig. 9, the frequency response of the experimental data was obtained using a Fourier transform, while the plots related to $G_o^v(\jmath\omega)$ and $K_{\text{ff}}(\jmath\omega)$ were obtained analytically, studying the frequency response of each system.

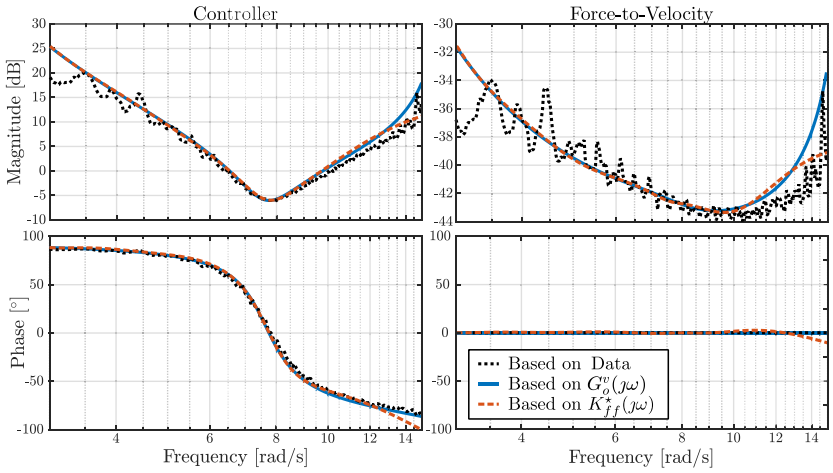

Fig. 9. Feedforward controller $K_{\rm ff}(s)$ approximation results in the frequency domain. The results with respect to the controller $K_{\rm ff}(\jmath\omega)$ and the force-to-velocity optimal mapping $T^{\rm opt}_{f_{ex}\to v}(\jmath\omega)$ are shown in (a) and (b), respectively.

A. Constraint Handling

A common issue in controlled WECs is that the controller often demands excessive device motion, or force, to achieve the theoretical optimal performance [1]. It is, thus, important to take limitations on the body motion or force into account in realistic controller implementation for the safety and lifetime of a WEC. As a result, several constraint handling mechanisms have been proposed in the literature.

An LTI amplitude displacement constraint handling strategy is proposed in [13] for the LiTe-Con, pursuing two main goals: 1) to preserve the essential zero-phase locking condition between $\tilde{F}_{\rm ex}(\omega)$ and $V(\omega)$ [32] and 2) to restrict the device velocity and displacement using a constant value $k \in [0, 1]$. Considering (10), including the constant value k, the force to velocity mapping is rewritten as

$$\mathcal{T}^{\rm opt}_{\tilde{f}_{\rm ex}\to v}(\jmath\omega) = k\frac{{\rm Re}\{G_o^v(\jmath\omega)\}^2 + {\rm Im}\{G_o^v(\jmath\omega)\}^2}{2{\rm Re}\{G_o^v(\jmath\omega)\}}. \quad (16)$$

Then, the gain multiplier, k, is used to ensure that physical constraints, defined in (7), on displacement and velocity are met. Then, the effect of the constant value k in (16) is transferred into the controller; thus, (11) can be redefined as

$$\mathcal{K}_{\rm ff}(\jmath\omega) = \frac{(2-k){\rm Re}\{G_o^v(\jmath\omega)v\} + k\jmath{\rm Im}\{G_o^v(\jmath\omega)\}}{2{\rm Re}\{G_o^v(\jmath\omega)\}}. \quad (17)$$

Note that, in (17), if $k = 1$, then $\mathcal{K}_{\rm ff}(\omega)$ matches the expression in (11). In addition, if $k = 0$, then, from (16), $\mathcal{T}_{\tilde{f}_{\rm ex}\to v}(\omega) = 0$.

From (11), (16), and (17), when the constraint handling mechanism is included, using the LTI approximation in (12), the control force can be expressed as follows:

$$F_u(\omega) = \underbrace{[kK_{\rm ff}(\omega) + (1-k)]}_{\text{Controller}}\tilde{F}_{\rm ex}(\omega). \quad (18)$$

Thus, the inclusion of the term k allows for the efficient implementation of velocity and, consequently, position constraints between zero and their theoretical maxima.

B. Transient Handling

To prevent adverse effects on the system performance due to estimation and controller transients, a "transient response remover" is implemented within the LiTe-Con framework, as follows:

$$f_{\rm uf}(t) = (1 - e^{-\alpha t})f_{\rm uc}(t) \quad (19)$$

where $f_{\rm uf}(t)$ denotes the actual control force applied to the system [see Fig. 1(b)] and α is a tuning constant. Here, α is determined empirically, during the experimental stage, as $\alpha = 0.1$, to smooth the first 15 s at the beginning of each experiment. However, for commercial WEC operation, start-ups of the device will be very infrequent, and the transient response remover is primarily utilized here to safeguard the prototype system.

Some comments regarding the transients handling mechanism, which allows for a smooth transition from the initially uncontrolled state to the normal controlled state, are worth highlighting. First, the initial time-domain transients, which can negatively impact the mechanical integrity of the prototype, are significantly reduced. Consequently, power generation is deprioritized, while the transient handling is active. However, taking into account the length of the experiments, the time during the transient handling is acting does not adversely affect the overall energy capture performance. Second, under the separation principle, the stability of the complete system, i.e., the controller, the wave excitation force estimator, and the WEC system, is guaranteed.

C. Estimator Design

Since the excitation force (which is required by the controller) is an immeasurable quantity for the moving WEC case [29], it has to be estimated based on other (measurable) quantities. The estimation strategy considered for this analysis estimates the wave excitation force acting on the device using only position measurements of the WEC. To this end, the state-space model of the WEC, as shown in (1) is extended,

based on the internal model principle [28], in order to include a description of the dynamics of the excitation force.

Considering that the wave excitation force can be described as

$$\begin{cases} \dot{x}_F(t) = A_F x_F(t) \\ \tilde{f}_{\text{ex}}(t) = C_F x_F(t) \end{cases} \tag{20}$$

where A_F and C_F are

$$A_F = \bigoplus_{p=1}^{\beta} \begin{bmatrix} 0 & \omega_p \\ -\omega_p & 0 \end{bmatrix}, \quad \text{and } C_F = [1 \quad 0 \cdots \quad 1 \quad 0] \tag{21}$$

containing all the natural frequencies, ω_p, of the harmonic oscillator, the Kalman Filter (KF), used in conjunction with the harmonic oscillator model in (20) (to describe the oscillatory dynamics of the wave excitation force), is, as shown in [29], one of the most accurate estimators among the different strategies available in the literature. In particular, the value for each ω_p is based on the spectral content of the wave. By way of example, when narrow-banded sea states are considered, as in the case of this study, where each wave is based on a JONSWAP spectrum, the peak component are used to define each ω_p. Thus, defining the augmented system as

$$\begin{cases} \dot{x}_a(t) = A_a x_a(t) - B_a f_u(t) \\ y(t) = C_a x_a(t) \end{cases} \tag{22}$$

with

$$\tilde{x}_a(t) = \begin{bmatrix} x(t) \\ \tilde{F}_{\text{ex}}(t) \end{bmatrix}, \quad A_a = \begin{bmatrix} A & BC_F \\ \mathbf{0} & A_F \end{bmatrix}$$
$$B_a = \begin{bmatrix} B \\ \mathbf{0} \end{bmatrix}, \quad C_a = [C \quad \mathbf{0}] \tag{23}$$

the continuous-time KF estimates the augmented state $x_a(t)$ as

$$\dot{\hat{x}}_a(t) = A_a \tilde{x}_a(t) + L_K(y(t) - C_a \tilde{x}_a(t)) \tag{24}$$

where the observer gain L_K is computed offline as the infinite horizon Kalman gain [28] and the estimation of $\tilde{f}_{\text{ex}}(t)$ is given by

$$\hat{\tilde{f}}_{\text{ex}}(t) = [\mathbf{0} \quad C_F]\hat{x}_a(t). \tag{25}$$

The interested reader is referred to [28] for a general discussion of sate-space observers and, in particular, Kalman-based estimators. Note that the estimator, as defined in (25), represents an unknown-input state observer. Thus, the observation gain can be computed using, for example, standard pole-placement approaches or, as the case of this study, LQG techniques, where the associated algebraic Riccati equations can be solved using well-established toolboxes [34].

D. Implementation

Fig. 10 shows the complete control structure used in this study, with the Kalman-based wave excitation force estimator, the constraint handling mechanism (dotted-green box), and a transient response remover (dashed-blue box). The extent of the controller components is indicated using a green dotted box.

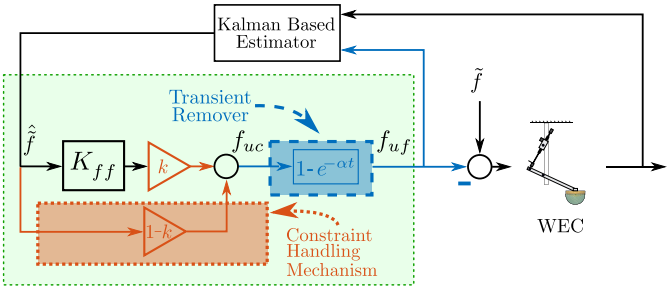

Fig. 10. Final control block diagram, including the Kalman-based estimator, the constraint handling mechanism (marked in orange), the transient remover (marked in blue), and the controller (marked in green). In addition, the components of both the target PC and the physical world are indicated.

TABLE II

SEA STATES USED IN THIS STUDY. THE SIGNIFICANT WAVE HEIGHT H_s AND PEAK PERIOD T_p ARE LISTED. A PEAK SHAPE PARAMETER $\gamma = 3.3$ IS USED IN ALL CASES

Sea State (SS)	H_s [m]	T_p [s]
SS1	0.0208	0.988
SS2	0.0625	1.412
SS3	0.1042	1.936

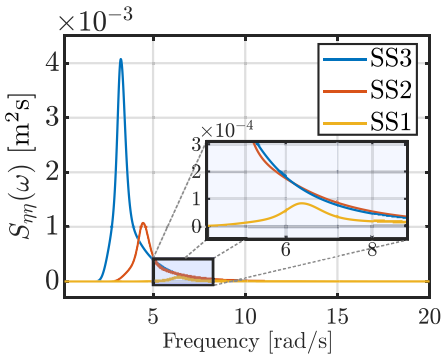

Fig. 11. Power spectral densities $S^1_{\eta\eta}(\omega)$, $S^2_{\eta\eta}(\omega)$, and $S^3_{\eta\eta}(\omega)$.

VI. CONTROLLER ASSESSMENT

In this section, the results for the complete control structure are shown, implementing the system, as described in Section V-D, in the hardware architecture outlined in Section II.

A. Sea States and Preliminaries

Inspired by Ringwood *et al.* [17], [18], three different irregular sea state (SS1–SS3), generated from JONSWAP-based spectral density functions, with peak shape parameter $\gamma = 3.3$ [35], are considered for the assessment. The significant wave height, H_s, and the peak period, T_p, are listed in Table II, for SS1–SS3. Fig. 11 shows the energy content of the three sea states by means of their power spectral density, denoted with $S^1_{\eta\eta}(\omega)$, $S^2_{\eta\eta}(\omega)$, and $S^3_{\eta\eta}(\omega)$ for SS1, SS2, and SS3, respectively.

From Fig. 11, it can be seen that the energy content of the three sea states is significantly different, with $S^1_{\eta\eta}(\omega)$ and $S^3_{\eta\eta}(\omega)$ being the least and most energetic sea states, respectively.

Unlike the controller, which can be designed for a set of sea states covered by a broadband frequency domain, the estimator, described in Section V-C, uses information about the oscillatory nature of the sea state. Thus, each T_p in Table II is employed to define the values ω_p in (21)

$$\omega_p = \frac{2\pi}{T_p}. \tag{26}$$

Then, the estimator is designed considering simultaneously the three values for T_p in Table II, which leads to a sixth-order A_f in (20). Thus, a single estimator for SS1, SS2, and SS3, is obtained instead of having one particular estimator for each sea state.

Furthermore, as described in [13], the value of k, in the constraint handling mechanism, is tuned using experimental exhaustive search, depending on each particular sea state considered in Table II.

Finally, for experimental implementation, both the controller and estimator, as discussed in Sections IV and V, respectively, are discretized using a zero-order-hold with, as previously mentioned in Section II, a sampling time of $T_m = 10^{-3}$ s. These discretized versions are implemented in the real-time execution architecture, as shown in Fig. 4.

B. Performance Assessment

As described in Section V-D and depicted in Fig. 10, the wave excitation force estimation and the control signal computation are performed in separated mathematical structures. Consequently, the assessment of the performance can be divided into two different stages: 1) estimation (see Section VI-B1) and 2) controller results (see Section VI-B2).[1]

1) Estimator: To assess the performance of the wave excitation force estimator, the calculation of a reference value for the "actual" wave excitation force is required, to determine the accuracy of the strategy. However, the actual excitation force is measurable only for a fixed device. Here, the $\tilde{f}_{\text{ex}}(t)$ reference is defined following the methodology adopted in [36] and [37]. A set of waves is generated in the wave tank, for which the device is fixed in its equilibrium position. Since the device is not moving, radiation and hydrostatic forces are zero so that the total force measured on the device, using the force sensor, is $\tilde{f}_{\text{ex}}(t)$. Thus, under ideal conditions (linear range and absence of noise for example), the force measured using standard load cells with a fixed-body approach perfectly matches the excitation force experienced by the body in a freely moving situation since the excitation force is independent of the motion of the body.

In Fig. 12(a)–(c), a comparison between the actual $\tilde{f}_{\text{ex}}(t)$ and estimated wave excitation forces $\hat{\tilde{f}}_{\text{ex}}(t)$ is shown. The estimation results are presented in Fig. 12(a)–(c) for SS1, SS2, and SS3, respectively.

There are some aspects, in Fig. 12, which are worth highlighting. The high-frequency content of $\hat{\tilde{f}}_{\text{ex}}(t)$ is clearly more

[1]For this study, the same wave realizations used for WECCCOMP [16], which are generated using filtered white-noise, are considered to permit direct comparability. Thus, the results shown in this section aim to stochastically show the performance of the controlled system in terms of the randomness of the wave.

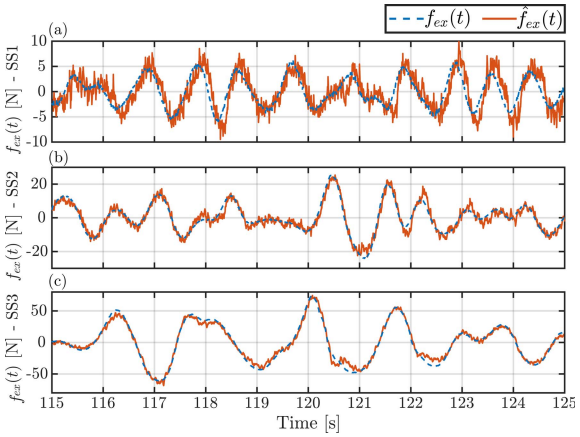

Fig. 12. Wave excitation force estimation results for SS1, SS2, and SS3. (a)–(c) Comparison of the actual and estimated time traces.

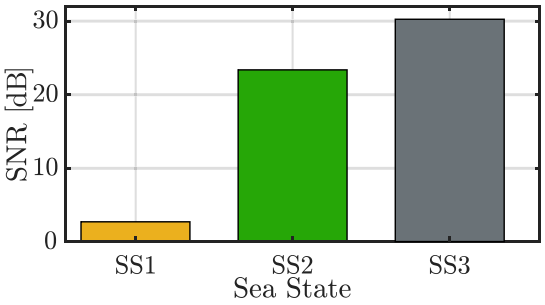

Fig. 13. SNR of each estimation is shown using dB.

visible with decreasing significant wave height H_s. To provide a quantitative measure of this effect, the signal-to-noise ratio (SNR) of each wave excitation force estimation is computed following:

$$\text{SNR}_i = \frac{\text{rms}\{\tilde{f}^i_{\text{ex}}(t)\}}{\text{rms}\{\tilde{f}^i_{\text{ex}}(t) - \hat{\tilde{f}}^i_{\text{ex}}(t)\}} \tag{27}$$

where $i \in \{1, 2, 3\}$ indicates the particular sea state SS1, SS2, or SS3, respectively; rms refers to the root mean square value of a signal, given as follows:

$$\text{rms}\{f(t)\} = \sqrt{\frac{1}{T}\int_0^T f(t)^2 dt} \tag{28}$$

where $T = 400$ s represents the length of the experiments.

The SNR, computed following (27) and expressed in [dB], for the wave excitation force estimation of SS1, SS2, and SS3, is shown in Fig. 13(b). It can be seen that the SNR improves (i.e., more signal, less noise) as the power of the sea states increases, which is in accordance with the qualitative observation in the time traces in Fig. 12(a)–(c). The observed behavior is mainly due to the noise added by the motor position sensor used for estimation. For the least energetic sea state SS1, with power spectral density $S^1_{\eta\eta}(\omega)$, the SNR is lower (higher noise content), and therefore, $\hat{\tilde{f}}_{\text{ex}}(t)$ is significantly noise-polluted. In contrast, for $S^3_{\eta\eta}(\omega)$, the device motion is larger, and hence, the SNR is higher, thus obtaining a less noisy $\hat{\tilde{f}}_{\text{ex}}(t)$.

Note that the noise and signal (force) levels, plotted in Fig. 12(a), have the same order of magnitude. Furthermore,

from Fig. 12(a), it can be noted that the actual and estimated wave excitation forces are slightly shifted. The shifting between the actual and estimated signals becomes negligible when the energy content of the sea state is increased. Finally, note that, even though the SNR improves when the power of the sea states increases, the noise level shows a consistent order of magnitude, which can be observed in the evolution from Fig. 12(a)–(c).

2) Controller: Concerning the results related to the controller performance, for each sea state SS1, SS2, and SS3, the experiments are run for 400 s. Then, the resulting energy, used as a performance metric for the controller, is computed as[2]

$$E_{\text{abs}}(t) = \int_0^t f_{\text{uf}}(\tau)\dot{x}_m(\tau)\,\mathrm{d}\tau. \tag{29}$$

To obtain a reference measure for the control performance, the force-to-position $G_o^x(s)$ and force-to-velocity $G_o^v(s)$ mappings, obtained in Section III, are considered to perform simulations using the actual wave excitation forces, obtained in the wave basin (see Section VI-B1), thus omitting the use of the estimator and avoiding the estimator errors and noise pollution of the excitation force signal. In addition, the controller $K_{\text{ff}}(s)$, in conjunction with both $G_o^x(s)$ and $G_o^v(s)$, is considered for the simulations in their continuous-time versions, instead of considering the discrete time version of the controller, as in the experimental implementation stage. In this scenario, the LiTe-Con is assumed to deliver ideal performance, thereby acting as a reference for the controller assessment.

By way of example, Fig. 14(a) and (b) shows a comparison of simulation and experimental time response of the system position $x_m(t)$ and the system velocity $v_m(t)$, respectively, considering the sea state SS3. Reference data are shown using orange dashed lines, while experimental data are shown in blue solid lines.

In Fig. 14, despite the high-frequency content in both the position and, mainly, the velocity data, good agreement between the simulation and experimental results can be observed. The obtained agreement is particularly highlighted in the main frequency component, given by the peak period of the sea state ($T_p = 1.963$ s for SS3; see Table II) and depicted, in Fig. 14, by the main oscillatory component.

Fig. 15 shows the resulting absorbed energy, following (29), for the three sea states SS1, SS2, and SS3. The plot contains the reference data (from simulation) and the experimental results.

A clear positive trend in energy absorption is shown for all three sea states, where SS3 shows the largest contribution of absorbed power (AP), which is measured by the slope of the resulting absorbed energy. SS2 and SS1 are then following in descending order. It is worth noting that, in Fig. 15, the AP for SS1, with respect to SS2 and SS3, is lowest, being, in practical terms, negligible. The poor performance of the LiTe-Con for SS1 is a consequence of the poor performance of the wave excitation force estimator, as shown in Figs. 12(a) and 13(b).

[2]Note that, the transient handling mechanism, defined in Section V-B, is considered in the computation of (29). However, considering that the transient handling mechanism only affects the first 15 s of 400 s of each experiment, its effect does not significantly impact the computed performance.

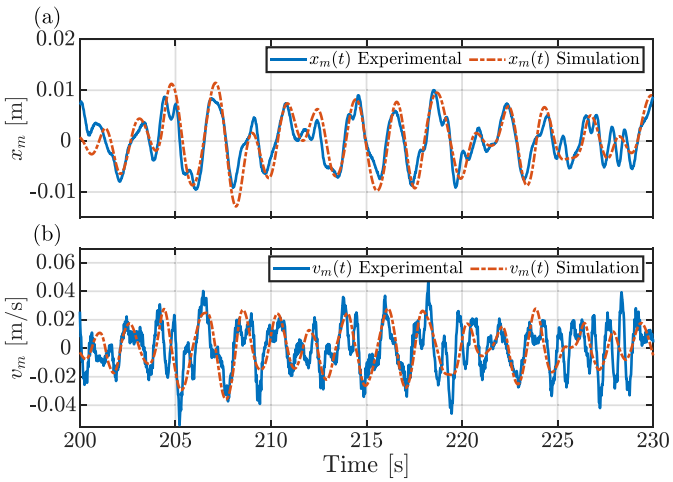

Fig. 14. Time traces with a comparison of simulation and experimental results for SS3. (a) Results for the system position $x_m(m)$. (b) Results for the system velocity $v_m(m)$. The simulation and experimental results are depicted with orange dashed and blue solid lines, respectively.

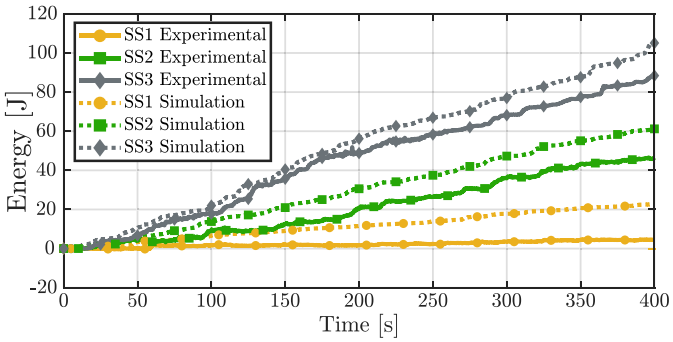

Fig. 15. Experimental resulting generated energy for SS1, SS2, and SS3.

For SS1, the estimated wave excitation force, used as input to the LiTe-Con (see Fig. 10), has a significant high-frequency content, induced by the noise from the position sensor. Furthermore, a slight phase shift between the actual and estimated wave excitation forces can be observed. Thus, since the controller behaves like a high-pass filter (see Fig. 9), the high-frequency content in the estimate has a considerable negative impact on the resulting performance. The lack of phase-matching between the actual and estimated wave excitation forces also contributes negatively to the resulting performance. The performance of the LiTe-Con for SS1 highlights the importance of good estimator performance, which plays a decisive role in the overall control performance.

Regarding the comparison of the simulated and experimental results, as depicted in Fig. 15, it can be observed that the experimental results show a lower performance compared to the reference (simulated) case. Considering the AP, as measured in Fig. 15 with the slope of the energy profile, the experimental efficiency, η_{exp}, computed as

$$\eta_{\text{exp}} = \frac{\text{AP}_{\text{exp}}}{\text{AP}_{\text{sim}}} \tag{30}$$

is obtained. With that, η_{exp} is 87.6%, 75.8%, and 19.7% for SS3, SS2, and SS1, respectively. Again, it is important to highlight the close connection between the efficiency results

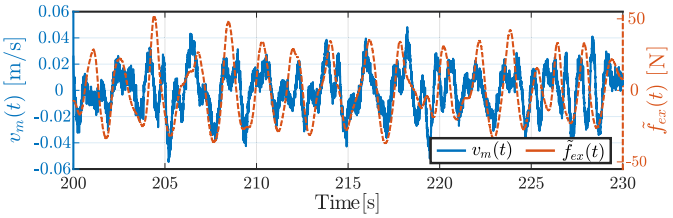

Fig. 16. Phase locking analysis for the system velocity, $v_m(t)$, and the wave excitation force, $\tilde{f}_{\text{ex}}(t)$, for SS3. The time traces are shown.

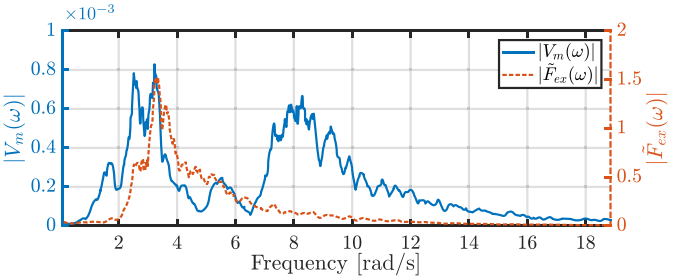

Fig. 17. Spectral analysis of the time traces in Fig. 16.

and the SNR, as shown in Fig. 13. Then, from the analysis of Figs. 12–14, the existing gap in Fig. 15, between simulation and experimental data, is a consequence of the presence of measurement noise. Such a measurement noise negatively impacts on wave excitation force estimation, as studied in [38], and its effect is then further exaggerate due to the high-pass characteristics of the LiTe-Con.

Considering the zero-phase locking condition[3] between the system velocity $v_m(t)$ and the wave excitation force $\tilde{f}_{\text{ex}}(t)$, which is an essential requirement for energy maximizing control design for wave energy systems, Figs. 16–18 show the phase locking analysis for $v_m(t)$ and $\tilde{f}_{\text{ex}}(t)$.

In Fig. 16, for the sea state SS3, the time traces for the system velocity $v_m(t)$ and the wave excitation force $\tilde{f}_{\text{ex}}(t)$ are shown using blue solid and orange dashed lines, respectively, for $t \in [200, 230]$ s. Qualitatively, Fig. 16 indicates phase matching between $v_m(t)$ and $\tilde{f}_{\text{ex}}(t)$. Then, considering the spectral analysis of the time traces in Fig. 16, $X_m(f)$ and $\tilde{F}_{\text{ex}}(f)$ are obtained, and their magnitudes, and $|X_m(f)|$ and $|\tilde{F}_{\text{ex}}(f)|$, are shown in Fig. 17. In Fig. 17, it can be seen that the spectral content of the wave excitation force is distributed within the energy band $\omega \in [1.25, 12.5]$ rad/s, which is driven by the JONSWAP spectrum of the wave $S^3_{\eta\eta}(\omega)$. With regard to the spectral distribution of the system velocity, $V_m(\omega)$, unlike the case of $\tilde{F}_{\text{ex}}(\omega)$, the energy is mainly contained within two different bands: the first band matches the energy band of the wave excitation force, while the second band is $\omega \in [6, 18]$ rad/s, due to the system dynamics. The first band, $\omega \in [1.25, 12.5]$ rad/s, is generated by the wave action on the system, while the second band, $\omega \in [6, 18]$ rad/s, is a consequence of the resonance of the system and unmodeled hydrodynamic and mechanical effects. To obtain a quantitative measurement of the phase-locking between $v_m(t)$ and $\tilde{f}_{\text{ex}}(t)$,

[3]Note that the strict real meaning of zero phase locking only applies for monochromatic signals.

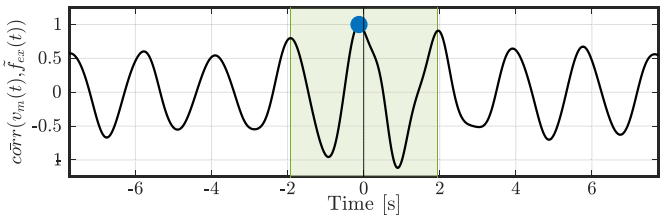

Fig. 18. Correlation analysis of the time traces in Fig. 16.

a cross correlation measure, defined as

$$R(\tau) = \text{cross}(v_m(t),\ \tilde{f}_{\text{ex}}(t)) \triangleq \int_{-\infty}^{\infty} v_m(t)\,\tilde{f}_{\text{ex}}(t+\tau)\,dt \quad (31)$$

is computed and then normalized by its maximum value

$$\overline{\text{cross}}(v_m(t),\ \tilde{f}_{\text{ex}}(t)) = \frac{R(\tau)}{\max\{R(\tau)\}}. \quad (32)$$

Fig. 18 shows the correlation analysis results for the time traces shown in Fig. 16. In Fig. 18, the area given by $\tau \in [-T_p, T_p]$ is indicated with a green-shaded-box. The maximum value of the correlation between $v_m(t)$ and $\tilde{f}_{\text{ex}}(t)$ is obtained when $\tau \approx -0.12$ s (indicated with a blue dot in Fig. 18), which represents a 6.2% of T_p for SS3 (see Table II). Thus, the location of the correlation maximum highlights the virtual zero-phase locking, obtained between the system velocity and the wave excitation force, achieved by the LiTe-Con. Note that, with the aim of analyzing the time shifting between velocity and excitation force, an equivalent alternative approach based on, for example, the coherence of the signals could be performed. Finally, the normalization performed with the max operator in (32) aims to simplify the understanding of the results shown in Fig. 18.

VII. Conclusion

This article documents the experimental implementation and validation of the recently proposed LiTe-Con [13]. Following a black-box approach, the control design model is initially identified from experimental data. Based on the identified model, the controller and a wave excitation force estimator based on a KF are designed. The performance of the excitation force estimate and the LiTe-Con are evaluated independently using the appropriate reference data.

With the presented results, this study validates the real-world performance of the LiTe-Con WEC controller, which addresses the energy maximizing control approach by means of a computationally tractable implementation. From the results, it can be seen that the presented control structure is easy to implement on realistic WEC systems, even using low-cost hardware architectures, such as low-cost microcontrollers, by nonspecialized technicians, requiring only a basic understanding of frequency response. From the implementation point of view, the LiTe-Con shows to be suitable to be implemented considering execution times of milliseconds (or less), while, at the same time, offering a constraint handling strategy.

In addition, from the estimation and control results, the strong connection between estimation and control performances of WEC systems is experimentally shown in this

study. Thus, the role played by the estimator in general WEC energy maximizing control problems is highlighted, showing that a good estimation performance is a prerequisite for good control performance. Furthermore, from the simulations in Section IV, the benefit of having an accurate wave excitation force estimation is reflected on the control performance achieved in simulations, used, in this study, as a benchmark for the experimental performance assessment.

From a general perspective, the implementation carried out in this study shows the experimental feasibility of a broadband LTI energy maximizing control solution, which considers constraint handling and is essentially based on system identification routines. In addition, in the complete control solution presented in this study, the simplicity and effectiveness, of the complete control structure and its implementability, are worth highlighting. However, considering that the LiTe-Con has not yet been extended to systems based on multiple WECs, to date, the general methodology presented in this study can only currently be considered for single WEC systems. The extension of the LiTe-Con to systems based on multiple WECs is a subject of future research.

Based on the simple implementation and the satisfying performance obtained in this study, the LiTe-Con shows the potential to make a significant contribution toward optimal control of commercially operating WECs, pushing the device performance beyond that of frequently used, suboptimal, passive, or reactive (spring/damper) type controllers.

REFERENCES

[1] J. V. Ringwood, G. Bacelli, and F. Fusco, "Energy-maximizing control of wave-energy converters: The development of control system technology to optimize their operation," *IEEE Control Syst.*, vol. 34, no. 5, pp. 30–55, Oct. 2014.

[2] U. A. Korde and J. V. Ringwood, *Hydrodynamic Control of Wave Energy Devices*. Cambridge, U.K.: Cambridge Univ. Press, 2016.

[3] L. Ljung, *System Identification–Theory for the User*. Upper Saddle River, NJ, USA: Prentice-Hall, 1999.

[4] N. Faedo, S. Olaya, and J. V. Ringwood, "Optimal control, MPC and MPC-like algorithms for wave energy systems: An overview," *IFAC J. Syst. Control*, vol. 1, pp. 37–56, Sep. 2017.

[5] W. E. Cummins, "The impulse response function and ship motions," *Schiffstechnik*, vol. 47, pp. 101–109, Mar. 1962.

[6] J. V. Ringwood, A. Merigaud, N. Faedo, and F. Fusco, "An analytical and numerical sensitivity and robustness analysis of wave energy control systems," *IEEE Trans. Control Syst. Technol.*, vol. 28, no. 4, pp. 1337–1348, Jul. 2020, doi: 10.1109/TCST.2019.2909719.

[7] R. H. Hansen and M. M. Kramer, "Modelling and control of the Wavestar prototype," in *Proc. 9th Eur. Wave Tidal Conf. (EWTEC)*, Southampton, U.K., 2011, pp. 163-1–163-10.

[8] P. Gieske, "Model predictive control of a wave energy converter: Archimedes wave swing," M.S. thesis, Delft Univ. Technol., Delft, The Netherlands, 2007.

[9] A. S. Zurkinden, F. Ferri, S. Beatty, J. P. Kofoed, and M. Kramer, "Nonlinear numerical modeling and experimental testing of a point absorber wave energy converter," *Ocean Eng.*, vol. 78, pp. 11–21, Mar. 2014.

[10] S. J. Beatty, M. Hall, B. J. Buckham, P. Wild, and B. Bocking, "Experimental and numerical comparisons of self-reacting point absorber wave energy converters in regular waves," *Ocean Eng.*, vol. 104, pp. 370–386, Aug. 2015.

[11] S. Giorgi, J. Davidson, M. Jakobsen, M. Kramer, and J. V. Ringwood, "Identification of dynamic models for a wave energy converter from experimental data," *Ocean Eng.*, vol. 183, pp. 426–436, Jul. 2019.

[12] J. Davidson, S. Giorgi, and J. V. Ringwood, "Identification of wave energy device models from numerical wave tank data—Part 1: Numerical wave tank identification tests," *IEEE Trans. Sustain. Energy*, vol. 7, no. 3, pp. 1012–1019, Jul. 2016.

[13] D. Garcia-Violini, Y. Pena-Sanchez, N. Faedo, and J. V. Ringwood, "An energy-maximising linear time invariant controller (LiTe-Con) for wave energy devices," *IEEE Trans. Sustain. Energy*, vol. 11, no. 4, pp. 2713–2721, Oct. 2020.

[14] L. Ljung, "Perspectives on system identification," *Annu. Rev. Control*, vol. 34, no. 1, pp. 1–12, Apr. 2010.

[15] J. Davidson, S. Giorgi, and J. V. Ringwood, "Linear parametric hydrodynamic models for ocean wave energy converters identified from numerical wave tank experiments," *Ocean Eng.*, vol. 103, pp. 31–39, Jul. 2015.

[16] (2020). *Wavestar Energy*. Accessed: Feb. 1, 2020. [Online]. Available: http://wavestarenergy.com/

[17] J. V. Ringwood *et al.*, "A competition for WEC control systems," in *Proc. 12th Eur. Wave Tidal Energy Conf.*, 2017, pp. 1–9.

[18] J. V. Ringwood *et al.*, "The wave energy control competition (WECCOMP): Wave energy control algorithms compared in both simulation and tank testing," *IEEE Trans. Control Syst. Technol.*, to be published.

[19] N. Tom, K. Ruehl, and F. Ferri, "Numerical model development and validation for the WECCCOMP control competition," in *Proc. ASME 37th Int. Conf. Ocean, Offshore Arctic Eng.*, 2018, p. V010T09A042, doi: 10.1115/OMAE2018-78094.

[20] C. Windt *et al.*, "Validation of a CFD-based numerical wave tank model of the 1/20th scale wavestar wave energy converter," *Fluids*, vol. 5, no. 3, p. 112, Jul. 2020.

[21] F. Ferri *et al.*, "A case study of short-term wave forecasting based on FIR filter: Optimization of the power production for the wavestar device," in *Proc. 22nd Int. Offshore Polar Eng. Conf.*, Rhodes, Greece, 2012, pp. 628–635.

[22] S. Beatty, F. Ferri, B. Bocking, J. Kofoed, and B. Buckham, "Power take-off simulation for scale model testing of wave energy converters," *Energies*, vol. 10, no. 7, p. 973, Jul. 2017.

[23] G. Bacelli, V. Nevarez, R. G. Coe, and D. G. Wilson, "Feedback resonating control for a wave energy converter," *IEEE Trans. Ind. Appl.*, vol. 56, no. 2, pp. 1862–1868, Mar. 2020.

[24] N. Faedo, G. Scarciotti, A. Astolfi, and J. V. Ringwood, "Energy-maximising control of wave energy converters using a moment-domain representation," *Control Eng. Pract.*, vol. 81, pp. 85–96, Dec. 2018.

[25] D. Garcia-Violini and J. V. Ringwood, "Energy maximising robust control for spectral and pseudospectral methods with application to wave energy systems," *Int. J. Control*, early access, doi: 10.1080/00207179.2019.1632491.

[26] F. Fusco and J. V. Ringwood, "A simple and effective real-time controller for wave energy converters," *IEEE Trans. Sustain. Energy*, vol. 4, no. 1, pp. 21–30, Jan. 2013.

[27] D. García-Violini, N. Faedo, F. Jaramillo-Lopez, and J. V. Ringwood, "Simple controllers for wave energy devices compared," *J. Mar. Sci. Eng.*, vol. 8, no. 10, p. 793, Oct. 2020.

[28] G. C. Goodwin *et al.*, *Control System Design*, vol. 240. Upper Saddle River, NJ, USA: Prentice-Hall, 2001.

[29] Y. Peña-Sanchez, C. Windt, D. Josh, and J. V. Ringwood, "A critical comparison of excitation force estimators for wave-energy devices," *IEEE Trans. Control Syst. Technol.*, vol. 28, no. 6, pp. 2263–2275, Nov. 2020, doi: 10.1109/TCST.2019.2939092.

[30] Mathworks. (2020). *MATLAB Simulink Real-Time*. Accessed: Apr. 21, 2020. [Online]. Available: https://uk.mathworks.com/help/xpc/

[31] J. Hals, A. Babarit, J. Krokstad, M. J. Muliawan, A. Kurniawan, and T. Moan, "The NumWEC project. Numerical estimation of energy delivery from a selection of wave energy converters," Norwegian Univ. Sci. Technol., Trondheim, Norway, Tech. Rep., 2015, doi: 10.13140/rg.2.1.3807.8885.

[32] J. Falnes, *Ocean Waves and Oscillating Systems: Linear Interactions Including Wave-Energy Extraction*. Cambridge, U.K.: Cambridge Univ. Press, 2002.

[33] N. Faedo, Y. Peña-Sanchez, and J. V. Ringwood, "Finite-order hydrodynamic model determination for wave energy applications using moment-matching," *Ocean Eng.*, vol. 163, pp. 251–263, Sep. 2018.

[34] The MathWorks. (2020). *icare: Implicit Solver for Continuous-Time Algebraic Riccati Equations*. Accessed: Nov. 1, 2020. [Online]. Available: https://la.mathworks.com/help/control/ref/icare.html

[35] K. Hasselmann, "Measurements of wind-wave growth and swell decay during the joint North Sea wave project (JONSWAP)," *Deutches Hydrographisches Institut*, vol. 8, p. 95, 1973.

[36] S. Giorgi, J. Davidson, and J. V. Ringwood, "Identification of wave energy device models from numerical wave tank data—Part 2: Data-based model determination," *IEEE Trans. Sustain. Energy*, vol. 7, no. 3, pp. 1020–1027, Jul. 2016.

[37] J. Hals, "Modelling and phase control of wave-energy converters," Ph.D. dissertation, Dept. Marine Technol., Norwegian Univ. Sci. Technol., Trondheim, Norway, 2010.
[38] F. Fusco and J. V. Ringwood, "A model for the sensitivity of non-causal control of wave energy converters to wave excitation force prediction errors," in *Proc. 9th Eur. Wave Tidal Energy Conf. (EWTEC)*, 2011. [Online]. Available: http://mural.maynoothuniversity.ie/3551/1/JR_Model_of_sensitivity.pdf

Demián García-Violini received the B.S. degree in automation and control engineering from the National University of Quilmes (UNQ), Buenos Aires, Argentina, in 2010, and the Ph.D. degree in engineering from the Buenos Aires Institute of Technology, Buenos Aires, in 2015.

He was a Post-Doctoral Researcher with the Centre for Ocean Energy Research, Maynooth University, Maynooth, Ireland, from 2018 to 2019. He is currently a Researcher with UNQ.

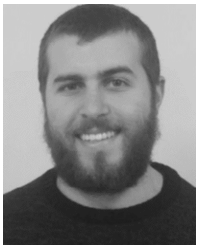

Yerai Peña-Sanchez received the Diploma degree in renewable energies engineering from the University of the Basque Country, Leioa, Spain, in 2016. He is currently pursuing the Ph.D. degree with the Centre for Ocean Energy Research, Maynooth University, Maynooth, Ireland.

He is working on the estimation and forecasting of wave excitation force.

Nicolás Faedo was born in Buenos Aires, Argentina, in 1991. He received the degree in automation and control engineering from the National University of Quilmes, Buenos Aires, Argentina, in 2015, and the Ph.D. degree in electronic engineering from the Centre for Ocean Energy Research group, Maynooth University, Kildare, Ireland, in 2020, with a focus on optimal control and model reduction for wave energy systems. In 2017, he joined the Centre for Ocean Energy Research group.

He was a Visiting Researcher with the Control and Power Group, Imperial College London, London, U.K., in 2018.

Dr. Faedo was a recipient of the 2019 ISOPE Best Student Paper Award and the Exxon mobile Prize and the finalist for the 2018 IFAC CAMS Young Author Award.

Christian Windt received the B.Sc. degree in mechanical engineering and the M.Sc. degree in energy systems from the Hamburg University of Technology, Hamburg, Germany, in 2013 and 2015, respectively. He is currently pursuing the Ph.D. degree, with a focus on high-fidelity numerical hydrodynamic modeling of wave energy systems, with the Centre for Ocean Energy Research, Maynooth University, Maynooth, Ireland.

He gained experience in the field of ocean wave energy conversion as a Visiting Research Student with Queen's University Belfast, Belfast, U.K., and the University of California at Berkeley (UC Berkeley), Berkeley, CA, USA.

Francesco Ferri received the master's degree in chemical and process engineering from the University of Bologna, Bologna, Italy, in 2008, and the Ph.D. degree in experimental and numerical modeling of wave energy converters from Aalborg University, Aalborg, Denmark, in 2014.

His research interests include hydrodynamic interaction in renewable energy offshore parks and control of wave energy converters.

John V. Ringwood (Senior Member, IEEE) received the Diploma degree in electrical engineering from the Dublin Institute of Technology, Dublin, Ireland, in 1981, and the Ph.D. degree in control systems from the University of Strathclyde, Glasgow, U.K., in 1985.

He is currently a Professor of electronic engineering with the National University of Ireland (NUI), Maynooth, Ireland, where he is also an Associate Dean for Engineering of the Faculty of Science and Engineering. His research interests cover time series modeling, wave energy, control of plasma processes, and biomedical engineering.